APL Materials

RESEARCH ARTICLE | JULY 17 2026

Resolving transient conductivity dynamics in phosphorus-implanted GeSn alloys using optical pump-terahertz probe spectroscopy

Simonas Driukas ; Chia-Ming Mai ; Ričardas Norkus ; Bronislavas Čehavičius ; Ignas Nevinskas ; Shang-Hua Yang ; Gintaras Valušis

Check for updates

APL Mater. 14, 071111 (2026)
https://doi.org/10.1063/5.0343680

View Online
Export Citation

Articles You May Be Interested In

Transferable GeSn ribbon photodetectors for high-speed short-wave infrared photonic applications

J. Vac. Sci. Technol. B (June 2024)

Local constrained expansion induced surface tensile strain and optical enhancement in suspended GeSn microstructures

Appl. Phys. Lett. (May 2026)

Demonstration of AlGaAs/GeSn p-i-n diodes

13 October 2026 07:58:21

AMERICAN ELEMENTS
THE MATERIALS SCIENCE MANUFACTURER®
Now Invent.™
29th ANNIVERSARY 1997 – 2026

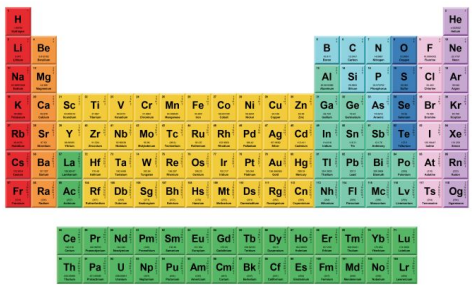

American Elements
Opens a World of Possibilities
...Now Invent!
www.americanelements.com
© 1997-2026. American Elements is a U.S. Registered Trademark

AIP Publishing

Resolving transient conductivity dynamics in phosphorus-implanted GeSn alloys using optical pump-terahertz probe spectroscopy

Cite as: APL Mater. 14, 071111 (2026); doi: 10.1063/5.0343680
Submitted: 20 May 2026 • Accepted: 29 June 2026 •
Published Online: 17 July 2026

View Online Export Citation CrossMark

Simonas Driukas,[1,a] Chia-Ming Mai,[2] Ričardas Norkus,[1] Bronislavas Čechavičius,[1] Ignas Nevinskas,[1] Shang-Hua Yang,[2,3,4,5] and Gintaras Valušis[6]

AFFILIATIONS

[1] Department of Optoelectronics, Center for Physical Sciences and Technology, Saulėtekio Ave. 3, LT-10257 Vilnius, Lithuania
[2] Institute of Electronic Engineering, National Tsing Hua University, Hsinchu City 300, Taiwan
[3] Department of Electrical Engineering, National Tsing Hua University, Hsinchu City 300, Taiwan
[4] Terahertz Optics and Photonics Center, National Tsing Hua University, Hsinchu City 300, Taiwan
[5] College of Semiconductor Research, National Tsing Hua University, Hsinchu City 300, Taiwan
[6] Institute of Photonics and Nanotechnology, Faculty of Physics, Vilnius University, Saulėtekio Ave. 3, LT-10257 Vilnius, Lithuania

[a] **Author to whom correspondence should be addressed:** simonas.driukas@ftmc.lt

ABSTRACT

GeSn alloys have garnered significant interest for electronic and optoelectronic applications over the past decade, primarily because of their monolithic compatibility with complementary metal–oxide–semiconductor fabrication platforms, tunable band structure, extended optical absorption into the short-wave infrared range, and excellent charge-transport properties. Recently, ion-implanted GeSn has been explored for the fabrication of photoconductive terahertz (THz) devices as a competitive alternative to low-temperature-grown III–V compound semiconductors. Since their ultrafast photoconductivity response governs the THz performance of such devices, this work provides a comprehensive characterization of the transient optoelectronic properties of ion-implanted GeSn alloys under different implantation doses and energies. In particular, optical pump–THz probe measurements were performed to assess the photoconductivity dynamics more accurately, while the Drude–Smith model was employed to extract the transient optoelectronic parameters of the samples under ultrafast excitation. Complementary characterization techniques, such as x-ray diffraction (XRD), photoluminescence (PL), and scanning electron microscopy (SEM), were also used to gain deeper insight into the properties of the ion-implanted GeSn samples. The results show that GeSn treated with moderate ion-implantation dose and energy exhibits an optimized balance between short carrier lifetime, good crystallinity, and high mobility, highlighting the importance of defect engineering for tailoring the transient optoelectronic properties of GeSn for ultra-broadband THz sensors. These findings are expected to support the development of next-generation GeSn-based functional devices.

© 2026 Author(s). All article content, except where otherwise noted, is licensed under a Creative Commons Attribution (CC BY) license (https://creativecommons.org/licenses/by/4.0/). https://doi.org/10.1063/5.0343680

I. INTRODUCTION

The growing need for digitization and development of smart devices operating at higher frequencies stimulates a search for new solutions for compact emission, advanced sensing, and 6 G wireless communication systems. A particular role here can be assigned to terahertz (THz) technology[1] with an operational frequency band spanning from hundreds of gigahertz (GHz) up to several THz. Employing such frequencies not only enables wireless communication with high data traffic[2,3] but also opens a prospective avenue in compact THz imaging and spectroscopy, including non-invasive medical screening, various materials inspection, and a

13 October 2026 07:58:21

variety of contactless industrial applications.[4] These developments inspire inquiry into semiconducting materials engineering that can serve as a core for innovative, astute gadgets. It is worth noting a wide range of semiconductor materials (including low-temperature grown GaAs, GaAsBi, InGaAs, and InAs structures) were used for THz time-domain spectroscopy,[5–8] InGaAs was also employed for compact THz emission from high electron mobility transistors[9] or resonant tunneling diodes[10] as well as for broadband and fast THz imaging applications.[11,12] Semiconducting GaAs/AlGaAs and InGaAs/InP nanostructures were main constituents in THz quantum cascade lasers;[13,14] GaN-based structures were found to be reliable and promising materials for compact THz plasmonic emitters[15,16] and sensitive THz detectors.[17,18] A distinguished place can be attributed to silicon as a key material for complementary metal–oxide–semiconductor (CMOS)[19] and BiCMOS technologies that can be extended for operation in the THz range and provide compact solutions for integrated circuits.[20]

Recently, a new material, germanium–tin alloys (GeSn), has been intensively investigated and discussed over a wide range of electronic and optoelectronic applications, owing to their monolithic compatibility with silicon-based CMOS fabrication processes, tunable band structures, extended sensitivity toward the short-wave infrared (SWIR) region, and superior carrier mobility.[21–25] Combining these parameters, applications of GeSn-based devices encompass advanced field effect transistors,[26,27] on-chip optoelectronic lasers,[28,29] mid-infrared sensors,[30,31] and photoconductive THz devices.[32–34]

Within this landscape, the development of GeSn-based THz devices has gained significant attention as a potential solution to the critical scalability and mass-production bottleneck in this field.[32,33,35] Although multiple applications have been accomplished via THz systems empowered by THz photoconductive devices, thanks to their high signal-to-noise ratio and ability to provide multidimensional information across both temporal and spectral domains,[4,36,37] existing THz photoconductive devices are still heavily dependent on low-temperature-grown III–V epitaxial films.[35,38–40] While these films require a specialized crystal growing process and often suffer from limited yield, GeSn thin films circumvent this limitation via their seamless compatibility with modern silicon-based platforms, thereby offering a pragmatic path for large-scale development and commercialization of THz technology.[21,22]

While GeSn alloys have been demonstrated as feasible ultrafast photoconducting materials for THz photoconductive devices, their optoelectronic properties and ultrafast carrier dynamics have been shown to play critical roles in their device performance.[32–34] In particular, it was demonstrated that phosphorus ion implantation is a viable approach to manipulate the sheet resistivity, carrier mobility, and carrier lifetime of GeSn material,[34] allowing, hence, to optimize the performance of the THz photoconductive detectors. Since sheet resistivity determines the dark current and the maximum optical power uptake of the device, while carrier mobility and lifetime govern its bandwidth, accurate characterization of these parameters is critical for the development of THz photoconductive devices.[7,33–35]

However, previous investigations often rely on Hall effect measurements and optical-pump–optical-probe (OPOP) spectroscopy to characterize these parameters, which can be indirect and can fail to correctly reflect the underlying THz generation and detection mechanism of the GeSn-based photoconductive devices. Whereas these devices are dependent on the transient photoconductivity attributed to femtosecond laser pulse excitation and the relaxation from the recombining excess photocarriers,[35] Hall effect measurements probe the DC steady state of the material,[41] and can likely underestimate the magnitude of carrier mobility due to grain boundaries.[42] Moreover, the probe beam used in OPOP spectroscopy can also excite additional photocarriers, therefore disturbing the system and providing a biased assessment of the dynamics unless a specialized design is employed.

In this work, we present the first, to the best of our knowledge, study on ultrafast carrier dynamics of phosphorus ion-implanted GeSn thin films using optical pump–THz-probe spectroscopy under different excitation conditions. First, investigating the GnSn structures with different ion-implantation energies revealed their effects on carrier dynamics via carrier lifetime estimates. Second, varying the optical pump wavelength enabled the excitation of carriers directly in the Γ valley, and the estimation of carrier trapping times into the implantation-induced defects. The optical pump–THz-probe approach grants us two major advantages. First, the unwanted disturbance from the probe beam is mitigated as the quantized photon energy of the THz wave (1 THz ⇔ 4.1 meV) is negligible, thus, to the bandgap of GeSn and that of the pump beam, thus enabling more accurate extraction of the carrier lifetimes in GeSn thin films. Second, THz waves have been demonstrated to determine carrier mobility, concentration, and sheet resistivity of photoexcited semiconductors.[43,44] Therefore, by recording the THz time-domain waveforms at various pump–probe delays, transient carrier dynamics can be resolved.[45–47] Moreover, varying the excitation conditions—optical pump excitation power and its wavelength—allowed to reveal the photoexcited carrier scattering effects, their dynamics, and transport properties in the range of fs-to-ns time-scale. Furthermore, complementary material characterization techniques, such as x-ray diffraction (XRD), scanning electron microscopy (SEM) measurements, and photoluminescence (PL) are conducted, aiming to provide a comprehensive physical insight into the crystallinity, bandgap structure, and the ultrafast conductivity characteristics of ion-implanted GeSn films. Collectively, these findings provide a practical and reproducible guideline for optimizing the ion-implantation parameters of GeSn thin films, paving the way for the development of high-performance, CMOS-compatible GeSn-based THz photoconductive devices with tailored ultrafast profiles.

II. METHODS

A. Sample preparation

An 8-in. intrinsic high-resistive silicon wafer (ρ >10 000 Ω·cm) serves as the substrate. Later, the Ge thin film as a virtual substrate (Ge-VS, 120 nm) underneath the GeSn thin film (150 nm) is grown on the Si substrate first. Finally, the GeSn alloy having 4% Sn composition was deposited via reduced pressure chemical vapor deposition (RPCVD, model: Epsilon 2000, ASM) on Ge-VS at a growth temperature under 350 °C.[33,34] The full wafer was then diced into multiple samples under test with a size of 10 × 10 mm^2 for further characterization. To manipulate the carrier lifetime and

13 October 2026 07:58:21

© Author(s) 2026

transient conductivity profile of the sample, ion implantation with phosphorus ions was conducted with various implantation dosages (5×10^{12}–5×10^{15} cm^{-2}, or 5×10^{12}–5×10^{15} for simplicity), under various implantation energies (10–200 keV).[34] For better benchmarking, an as-grown GeSn sample (denoted as "intrinsic") and another sample whose GeSn layer was completely etched out by dry etching (denoted as "substrate") are included with their transport properties for comparison. The former sample can provide insights into the effects of ion implantation under various material conditions, while the latter serves as the control group to isolate the contribution of GeSn layers during the optical excitation. For better readability, the ion-implanted samples are denoted by their respective ion implantation dosages and implantation energy. For example, 5×10^{12}, 50 keV refers to the GeSn sample treated with a dosage of 5×10^{12} cm^{-2} and energy of 50 keV.

Note that none of these ion-implanted samples are treated with thermal annealing deliberately. Although it is a common post-implantation technique allowing the restoration of crystallinity in solid-state studies, thermal annealing could also lengthen the carrier lifetimes of the sample, which is unfavorable for THz photoconductive devices. Furthermore, the process would also activate the dopants, thereby elevating the dark conductivity level of the material. This effect leads to unwanted absorption of THz radiation and could harm the performance of the fabricated THz photoconductive devices.

B. Photoluminescence

Room temperature photoluminescence measurements were performed using a 532 nm diode-pumped solid-state laser, with the excitation intensity kept at around 5 kW/cm^2. The photoluminescence was detected by a thermoelectrically cooled InGaAs-based photodetector in reflection mode using a lock-in amplifier, recording the chopped signal at 200 Hz frequency.

C. High resolution x-ray diffraction and scanning electron microscopy

Since ion implantation can influence the crystallinity of the GeSn thin films, which notably affect the transient conductivity profiles of the samples, we performed high-resolution x-ray diffraction (HR-XRD, model: SmartLab diffractometer, Rigaku Corporation) to evaluate the structural quality of the samples. The x-ray wavelength was generated with Kα_1 radiation from a copper anode, whose wavelength was 1.5406 Å. The high-resolution $\theta - 2\theta$ XRD scans were then performed over an angular range of 62° to 72° with a step size of 0.02°, at the scanning speed of 10° per minute. These scans were recorded along the out-of-plane normal of the samples under ambient conditions. Three samples - 5×10^{15} 50 keV, substrate, and intrinsic GeSn were also selected for additional inspection by SEM to probe the thickness and surface of the CVD-grown films. A "FEI Helios NanoLab 650" SEM system was used, combined with Ga focused ion beam (FIB) etching to reveal the layered sample structure and thickness of Ge/GeSn layers.

D. Optical pump–THz probe spectroscopy

A detailed study of carrier relaxation dynamics was performed using the optical pump–THz probe (OPTP) technique under varying excitation conditions, namely, different optical pump powers and excitation wavelengths. The schematic diagram of the experimental setup is shown in Fig. 1.

A ytterbium-doped potassium gadolinium tungstate (Yb:KGW) "Light Conversion PHAROS" laser was used for both the optical pump and the THz emitter–detector branches. The laser delivered pulses at 1030 nm with a duration of 150 fs and a repetition rate of 200 kHz, and the beam was split into two branches. The first branch was used to pump the THz emitter and detector, whereas the second was directed through an "ORPHEUS" optical parametric amplifier (OPA) (Light Conversion, Vilnius, Lithuania),

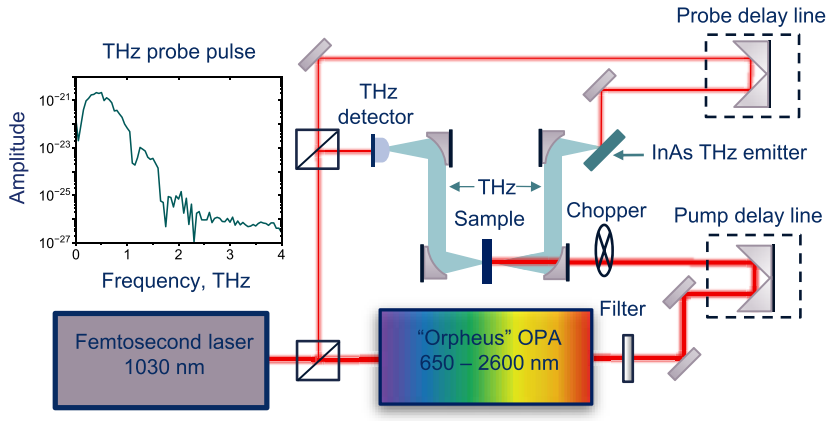

FIG. 1. Schematic of the experimental optical pump–THz probe setup and the spectra of THz probe pulse. The seed laser pulse was split into two branches: one for THz generation and probing and the other for optical pumping of the sample. For pump–probe measurements, the THz delay line was fixed at the position of maximum probe signal, while the pump beam was mechanically chopped and moved in time with a delay line to measure the decay kinetics via lock-in detection. For THz pulse acquisition and photoconductivity extraction, the chopper was placed in the THz emitter pump line, and the probe delay line was scanned to record the complete THz waveform in the time domain with and without optical excitation of the sample. The excitation time delay in this case was set at the maximum transmission attenuation point.

13 October 2026 07:58:21

© Author(s) 2026

which enabled both amplification of the radiation and tuning of the wavelength over the range from 650 to 2600 nm while keeping the pulse duration of 150–200 fs. This made it possible to excite the samples at different photon energies and to investigate hot-carrier effects, inter-valley dynamics, and selective excitation of different heterolayers. However, the laser output power decreased with increasing wavelength; therefore, excitation at longer wavelengths was performed at lower pump power. A GaAsBi-based "Teravil" THz photoconductive antenna detector was employed for lock-in detection of the differential THz signal in combination with optical chopping at 576 Hz of the excitation beam, while the photoexcited InAs surface served as the THz emitter. Probe delay line was kept stationary at the position of maximum THz signal value, while the pump delay line was swept to acquire a transient trace of excitation and decay of pump-induced THz probe transmission change.

E. Extraction and analysis of transient conductivity from optical pump–THz probe

In this study, in addition to the optical pump–THz probe scanning on the pump delay line, we also scanned the whole THz waveform on the THz delay line, to further investigate the transient conductivity profiles of the samples. As a preliminary study, we only performed THz scanning at the maximum attenuation point of each sample, where the photoinduced conductivity profiles are the most prominent and representative. Note that due to different conductivity profiles within the samples, the exact positions of the THz scanning on the pump–probe axis among the samples are independent.

As the main pump wavelength is centered at 1251 nm, falling outside the absorption region of intrinsic Si, we expect the majority of photons to be absorbed in GeSn and Ge-VS layers, thus forming an optically thin conductive layer on top of a semi-insulating substrate. Noting that given a THz pulse propagates through the sample with normal incidence, the Tinkham equation is a suitable analytical solution to extract the transient photoconductivity $\Delta\tilde{\sigma}(\omega,\tau)$ of the optically excited GeSn layer,[48,49] explicitly given as the following expression (1):

$$\Delta\tilde{\sigma}(\omega,\tau) = -\frac{n_{sub}+1}{Z_0\, d}\frac{\Delta\tilde{E}(\omega,\tau)}{\tilde{E}_0(\omega)}, \tag{1}$$

where $\Delta\tilde{\sigma}(\omega,\tau)$ denotes the transient complex photoconductivity at angular frequency ω and pump–probe delay τ, n_{sub} denotes the refractive index of the substrate (for Si, $n_{sub} \sim 3.418$),[50] Z_0 stands for the free space wave impedance (~377 Ω), and $\Delta\tilde{E}(\omega,\tau)$ and $\tilde{E}_0(\omega)$ refer to complex spectral magnitude of differential electric field and that without illumination, respectively. Assuming that the contribution from two-photon absorption in Si is negligible,[51] both GeSn and Ge-VS should be photo-excited, and this shapes the transient conductivity profile. Thus, we take the thickness d = 270 nm, which is the sum of the thickness of the GeSn and Ge-VS layer for all samples that excludes the substrate in the following calculation.

In addition to the extraction of the transient conductivity itself, more insights regarding the carrier dynamics can be revealed via fitting the conductivity to a suitable macroscopic charge transport model. In this research, due to the possible carrier localization effect in the GeSn epitaxial thin film due to ion implantation, the Drude–Smith model is deployed to explain the transient complex conductivity when carrier backscattering is significant.[52] The formulation of the Drude–Smith model used in this study is defined as in (2),

$$\tilde{\sigma}(\omega) = \frac{\sigma_0}{1-i\omega\tau}\left(1+\frac{c}{1-i\omega\tau}\right). \tag{2}$$

There are three fitting parameters in Eq. (2): σ_0 denotes the intrinsic DC conductivity, τ is the carrier scattering time, and c labels the backscattering coefficient constrained between 0 and −1. A value of c close to 0 means that the carriers could move in the material freely, resembling the carrier transportation behavior of an ideal metal, and the Drude–Smith model truncates to the conventional Drude model. On the contrary, c value approaching −1 indicates significant carrier backscattering or localization, causing a reduction in the macroscopic conductivity, as described by the second term in Eq. (2). Therefore, as an extension to the classic Drude model, the Drude–Smith model illustrates the picture where the conductivity of the samples is dominated by carrier transport driven by THz electric field, but, instead of moving completely freely in the medium, the movements of the carriers are, in fact, partially limited by lattice boundaries, defects, or traps. These restrictions further shape the conductivity profile and are quantized by the backscattering coefficient c in the Drude–Smith model. As this picture highly resembles the expectation of microscopic conductivity origin in ion-implanted GeSn, we deploy the Drude–Smith model in this study to explain the conductivity characteristics of our samples.

Furthermore, from the Drude–Smith fitting parameters, electrical constants, such as macroscopic DC conductivity σ_{DC}, macroscopic mobility μ, and photocarrier concentration N_e, can be extracted to provide additional insight to the properties of the material under ultrafast optical excitation, through Eq. (3) through (5),[53]

$$\sigma_{DC} = \sigma_0\,(1+c), \tag{3}$$

$$\mu = \frac{q\,\tau\,(1+c)}{m^*}, \tag{4}$$

$$N_e = \frac{\sigma_0\, m^*}{q^2\,\tau}, \tag{5}$$

where q stands for the elementary charge and m^* is the effective mass of the carriers in the material. Here, as our 4% Sn concentration GeSn has not crossed the transition boundary from indirect to direct bandgap material, which often occurs when Sn concentration exceeds 8%–10%,[54,55] we assume that its effective mass resembles that of Ge and the majority of the carriers are still excited to the L-valley. In addition, due to strong anisotropy in the L-valleys of Ge, one must consider its conductivity effective mass, which is given by the weighted harmonic average of the longitudinal mass m_l^* and transverse mass m_t^*,[56]

$$\frac{1}{m^*} = \frac{1}{3}\left(\frac{1}{m_l^*}+\frac{2}{m_t^*}\right). \tag{6}$$

Substituting $m_l^* = 1.64\ m_0$ and $m_t^* = 0.082\ m_0$,[57] we obtain the conductivity effective mass of GeSn $m^* = 0.12 m_0$, where $m_0 = 9.1 \times 10^{-31}$ kg is electron mass.

13 October 2026 07:58:21

© Author(s) 2026

III. RESULTS AND DISCUSSION

A. Structural characterization

As the first characterization step, three samples were selected for imaging with SEM: intrinsic GeSn, substrate, and 5×10^{15} 50 keV sample. The acquired surface and edge microscopic images are displayed in Fig. 2. A distinct feature is observed in all selected samples: around 400 nm wide pyramid-like crystalline shapes. We believe that the cause of this may be the precipitation of Ge into small monocrystals, as they are present even in the substrate sample, where the GeSn layer is etched away, and only Ge on the Si substrate remains. Apart from that, no key differences in major surface crystalline structure are seen between doped and undoped Ge samples. Only the substrate sample shows increased surface roughness due to wet etching.

Looking into the thickness of the layers, a clear difference is seen between the etched substrate sample and intrinsic GeSn, which is around 150 nm thicker. However, no visual differences in GeSn and Ge layers can be seen; only the combined thickness of Ge buffer and GeSn layers is measured at 280 nm, which is in good agreement with the sample growth target of 270 nm.

Following the SEM analysis, the XRD spectra of all the studied samples were recorded and are shown in Fig. 3, where three peaks can be clearly observed. Starting from right to left, the three peaks are located near 65.32°, 66.14°, and 69.15° for the intrinsic sample. Given the wavelength, we can calculate the corresponding lattice constants, which are 5.7096, 5.6467, and 5.4296 Å, respectively. While the latter two are in good agreement with reported values of lattice constants of Ge (5.658 Å)[58] and Si (5.431 Å),[59] we can infer that the three peaks stand for GeSn, Ge, and Si, from left to right, respectively.

After the characteristic peaks are identified, one can observe that compared to the intrinsic sample, the 5×10^{15} 50 keV sample has almost lost its GeSn peak. In addition, although all three distinct peaks can still be observed from the 5×10^{12} 50 keV and 5×10^{12} 100 keV samples, a notable intensity drop and peak position shift can be found. These phenomena could be well explained by the implantation energy and dosage of ion implantation, as higher implantation dosage and lower implantation power yield dense distribution of the ions. Since these samples did not go through annealing to repair the damage from ion bombardment, intensity degradation of the peaks implies crystallinity loss of the lattice.

In addition, we estimated the projected range of the implanted phosphorus ions. Because the Sn fraction in our GeSn alloy is relatively low, the ion stopping power of the material is predominantly

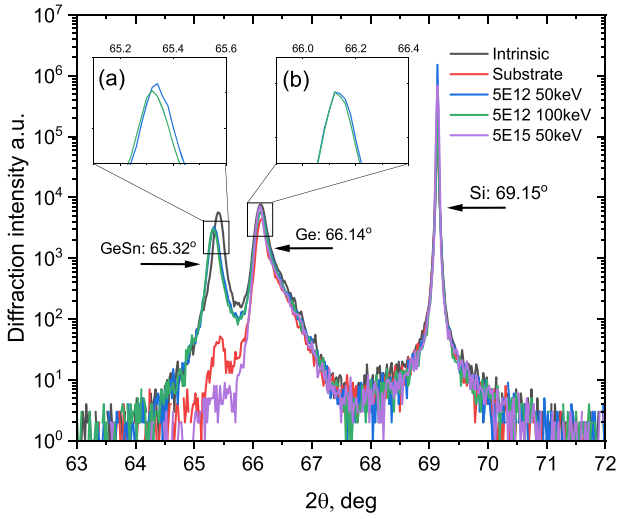

FIG. 3. XRD spectra of all studied samples. The three peaks, situated at roughly 65.32°, 66.14°, and 69.15°, are indicated by the arrows, corresponding to GeSn, Ge, and Si, respectively. Insets [(a) and (b)] indicate zoomed-in peak positions of Ge and GeSn with 5×10^{12} doping. Note the slightly smaller peak intensity of the higher implantation energy sample at inset (a), while the underlying Ge buffer remains effectively the same as seen in inset (b).

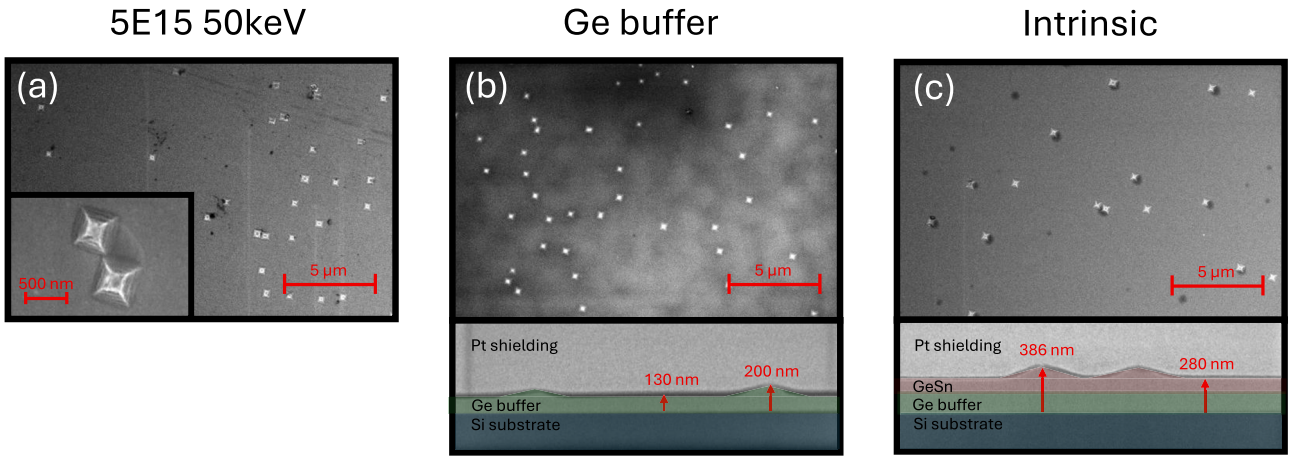

FIG. 2. SEM images of selected samples: (a) 5×10^{15} and 50 keV ion-implanted sample, (b) substrate sample, and (c) intrinsic GeSn. The inset in panel (a) depicts the close-up view of the pyramid-like crystalline structures visible on the surface of all imaged samples. The insets in panels [(b) and (c)] display side images of locally Ga ion-etched holes with a sputtered Pt shielding on top to protect the top layer from etching. The coloring of layers seen in these insets is purely for visual indication. No characteristic contrast differences were observed between GeSn and Ge buffer layers.

13 October 2026 07:58:21

© Author(s) 2026

governed by the host Ge matrix. We can, therefore, approximate the spatial distribution by referencing established depth profiles of P-implanted Ge. According to the literature,[60] projection range of P ions into Ge is experimentally characterized as ~70 nm, while simulation results indicate a penetration depth of less than 100 nm even with 100 keV implantation energy. Given the thickness of our GeSn thin film is 150 nm, we can conclude that the majority of the dopants are confined within the GeSn layer. This is also empirically supported by the XRD spectra in Fig. 3, where the Ge peak intensities from all GeSn samples remain virtually identical regardless of implantation settings. From here, we can confirm that the GeVS layer is almost intact with the implantation settings used in this study, and the spatial distribution of the implanted ions is exclusively localized within the GeSn layer.

B. Optical characterization

To get deeper insight into the ion-implanted RPCVD-grown GeSn material, photoluminescence (PL) spectra were recorded (Fig. 4). As can be seen, only the undoped intrinsic sample showed significant PL above the noise floor. For other samples, no clear PL peaks are visible, as displayed in the bottom panel of Fig. 4. The Ge buffer, being a strictly indirect band-gap material, produced no emission. On the other hand, in the ion-implanted samples, the emission is most likely strongly quenched by the introduced trap states; therefore, it can be a reason why no PL can be seen.

Still, the emission peak at 0.676 eV of the intrinsic sample confirms the presence of GeSn. Moreover, the shape of the PL curve is clearly asymmetric, with the PL emission extending into the lower energy regions. A reason for this could be the combined emission from both Γ and L valleys, of which the energy difference rapidly decreases with increasing Sn concentration and reaches a direct–indirect transition at 6%–10%.[31,55,61] The band-to-band transition energies to Γ and L valleys can be calculated using the empirical GeSn bandgap equation for each valley,[31]

$$E_g^{\xi}(Ge_{1-x}Sn_x) = (1-x)E_g^{\xi}(Ge) + xE_g^{\xi}(Sn) - b_{\xi}x(1-x), \quad (7)$$

where ξ represents either the Γ or L valley and b represents the Bowing parameter. For the 4% Sn concentration present in the studied sample group, the calculated transition energies are E_g^{Γ} = 0.675 eV (for a b = 1.95, which is in the range of reported values[61]) and E_g^{L} =0.61 eV (b = 0.89[31]). Noticeably, they lie very close to the emission peak and the lower energy shoulder of the PL, giving strong evidence for the combined emission of both Γ and L valleys as an explanation for the asymmetrical shape of the PL spectrum. Normally, the indirect L valley should display a very weak or no PL signal. However, the close presence of the Γ valley could facilitate an inter-valley crossing of a large portion of the excited carriers, resulting in detectable emission from both direct and indirect valleys. The same phenomenon is likely present in the doped samples, but due to a higher concentration of traps, the PL is unmeasurable. Nevertheless, the existence of close proximity Γ and L valleys and the impact of ion implantation can be further probed by analyzing the kinetics of photo-generated charge carriers, as will be shown below.

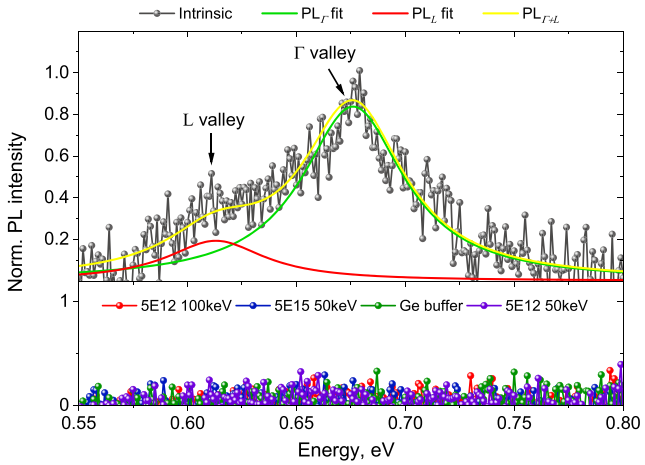

FIG. 4. Photoluminescence spectra of GeSn samples. The upper graph displays the intrinsic sample spectra, while the lower displays the rest of the samples. Note the PL peak shoulder extending into the lower energies, possibly caused by dual valley emission. The spectra were fitted as a sum of a Lorentzian function of two peaks (yellow curve) at center energies of 0.61 eV (indicated as L valley, red spline curve) and 0.675 eV (Γ valley, green spline curve).

C. Kinetic analysis

1. Carrier lifetime characterization

Despite the considerable attention devoted to investigating carrier dynamics in GeSn alloys, ranging from bulk MBE-grown materials to monocrystalline and CVD-grown films, most studies report intrinsic GeSn carrier lifetimes ranging from several hundred picoseconds to several nanoseconds.[62–64] While this indicates high material quality suitable for steady-state optoelectronic applications, it limits the material's applicability at THz frequencies. Post-processing by ion implantation substantially reduces the carrier lifetime, as demonstrated by Chen *et al.*[34] The OPOP spectroscopy applied in this study risks unintentionally disturbing the carrier dynamics via secondary optical excitation from the probe beam. Here, we use an optical pump–THz probe approach, which is directly sensitive to the concentration of photogenerated carriers, to gain deeper insight into the carrier dynamics of doped GeSn films and their characteristic relaxation times. Moreover, key photoconductivity and mobility parameters can also be evaluated.

TABLE I. Carrier decay fit results of experimental optical pump–THz probe data. A mono-exponential model was used to describe the kinetics within the measured timescale.

Sample	τ[a] (ps)	A[b]
Intrinsic	132	8.5
Ge buffer	120	2.55
5×10^{12}@50 keV	8.3	6.25
5×10^{12}@100 keV	4.5	3.08
5×10^{15}@50 keV	5.5	2.35

[a] τ—characteristic decay time constant.
[b] A—decay amplitude.

13 October 2026 07:58:21

© Author(s) 2026

The kinetic analysis performed by optical pump–THz probe spectroscopy reveals carrier lifetimes on the order of picoseconds for the ion-implanted samples and much longer lifetimes of more than one hundred picoseconds for the intrinsic samples. Curve fitting was performed to extract the decay parameters presented in Table I. A mono-exponential model with a constant baseline was applied, since bi-exponential fitting yielded a second, longer-lived component with a negligibly small or even negative amplitude in order to achieve convergence of the fit residuals. This behavior is most likely caused by weak excitation and decay of the underlying Ge buffer layer, which has a carrier lifetime in the μs range[65] and, therefore, appears as a constant baseline on the measured timescale.

The experimental data and the theoretical fits are presented in Fig. 5. As can be seen, the rise time of the induced THz transmittance transient is relatively long in all investigated structures, extending over several picoseconds. However, the decay behavior of the intrinsic sample and the Ge buffer is in sharp contrast to that of the ion-implanted structures: the intrinsic and Ge buffer samples exhibit substantially longer decay times, exceeding 17 ps. These features can be explained by the complex multivalley nature of the Ge conduction band:[66] electrons excited to high-energy states in the

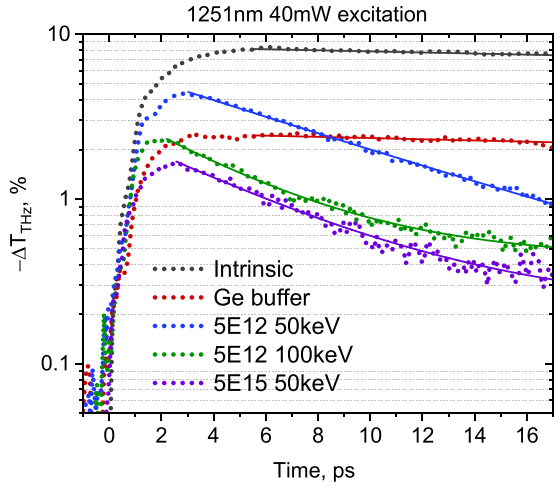

FIG. 5. Charge-carrier decay measured by the optical pump–THz probe technique. The change in THz probe absorption is represented by percentile decrease in sample transmission upon optical excitation. The experimental data are shown as dotted lines, while the solid curves represent the mono-exponential fits.

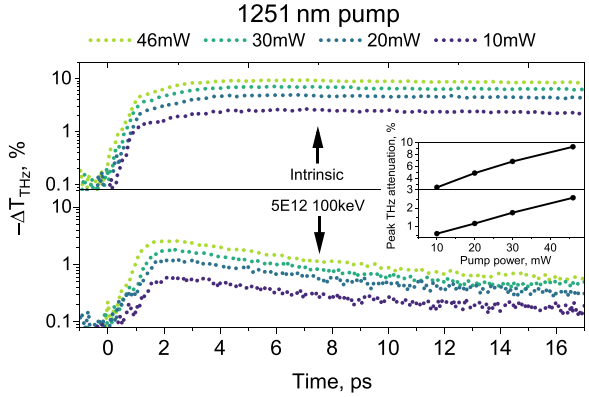

FIG. 6. Optical pump–THz probe decay kinetics measured at different optical pump powers for intrinsic GeSn and 5×10^{12} 100 keV doped GeSn. Note the long decay time in the intrinsic samples and the exponential decay in the doped sample. No clearly resolved differences are observed varying the excitation power, except for an increase in absorption with the pump intensity. The insets on the right of each panel denote the peak THz absorption change with the increase in the optical pump power.

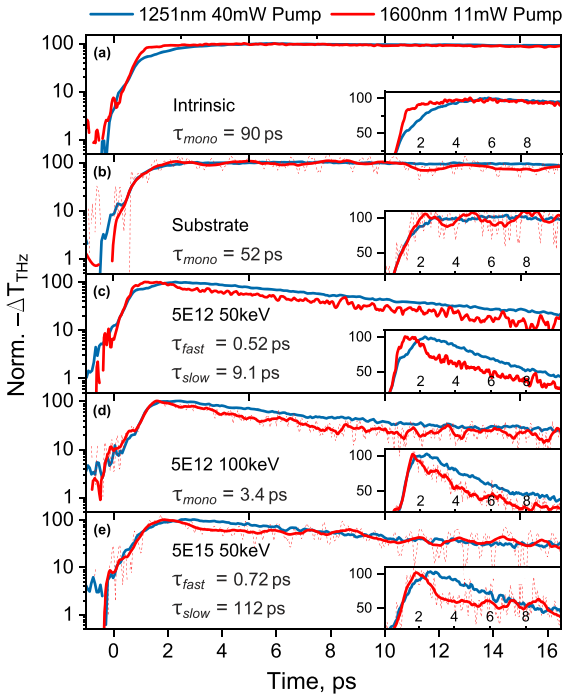

FIG. 7. Normalized transient THz absorption of all of the samples at two different optical pump wavelengths—1251 nm 40 mW (blue curve) and 1600 nm 11 mW (red curve). Due to low signal-to-noise ratio, some of the measured curves were additionally smoothed for visual clarity and represented as continuous lines, while the experimental data are left as dashed ones. Kinetics were also modeled as mono- or bi-exponential decay functions depending on the sample. The characteristic fast, slow, or mono-exponential time constants are written within the graphs. The right insets in each graph show zoomed decay in the first 10 ps. A linear scale is chosen to resolve the emerging differences more thoroughly. Note that in the intrinsic sample at 1600 nm wavelength excitation, the rise in THz attenuation is faster because the majority of carriers are generated directly to the Γ valley. Note the changes appearing in the initial 3 ps at 1600 nm wavelength—a faster rise time followed by a faster decay in the ion-implanted GeSn when comparing to the 1251 nm wavelength pump. The smooth peak in the inset of panel (c) can be attributed to the electron localization in the Γ valley, and the further rapid decrease is related to its transfer to the ion-implantation-induced defects and following recombination. Higher implantation energies induce more defects, resulting in shorter carrier lifetimes [inset of panel (d)]; higher doping at 50 keV implantation energies does not mask the smooth peak [panel (e)] visible at 1600 nm wavelength excitation, which is followed by rapid, about 1 ps duration escape from the Γ valley. The extended long relaxation tail can be related to electron intervalley transfer effects and enhanced scattering rates at high doping concentration.

13 October 2026 07:58:21

© Author(s) 2026

central Γ valley are first scattered into the subsidiary Δ valley and finally relax into the lowest-lying L valley. Note that the Ge buffer exhibits lower THz absorption and shorter carrier lifetimes compared with typical values reported for Ge.[65] This may be explained by the increased surface roughness observed in Fig. 2 and defects introduced by wet etching of the top GeSn layer. In contrast to the long rise and decay of THz absorption in intrinsic and substrate samples, the ion-implanted samples exhibit markedly different decay dynamics. Owing to dominant trap-assisted recombination of photoexcited carriers, the carrier lifetime is shortened, and the signal amplitude is suppressed. As expected, the lower implantation energy and concentration resulted in a slightly longer characteristic carrier decay time of 8.3 ps compared with the other doped samples. The remaining two samples show several distinct differences. Although both exhibit reduced carrier lifetimes and lower signal amplitudes, the higher implantation energy of 100 keV appears to produce a faster decay of 4.5 ps, compared with 5.5 ps for the sample with the higher ion concentration. For this case, a longer carrier decay is observed despite that the higher dopant concentration may indicate overdoping-induced degradation of the bulk crystal structure, as evidenced by the XRD spectra shown in Fig. 3. The resulting partially amorphized GeSn state is expected to exhibit enhanced carrier backscattering and significantly reduced mobility, thereby promoting carrier localization and prolonging the decay of the THz absorption signal.

Next, the optical pump–THz probe measurements were repeated with varying optical pump power from 10 mW up to 46 mW (excitation densities are from 0.7 $\times 10^{17}$ to 3.22×10^{17} cm^{-3}, respectively) for two selected samples—intrinsic GeSn and 5×10^{12} 100 keV doped GeSn. As can be seen in Fig. 6, apart from the decrease in THz absorption amplitude, no characteristic differences can be distinguished between the kinetics acquired with different pump power for the doped sample as well as the intrinsic one, indicating that the effect of carrier screening in the measured decay curves can be neglected.

Moreover, the usage of the "ORPHEUS" parametric amplifier as the pump source also allowed us to extend the investigation by selecting a different excitation wavelength. A 1600 nm wavelength (0.775 eV) pump was selected in addition to that of 1251 nm to excite mainly the GeSn layer while minimizing the excitation of the Ge buffer. The results of decay kinetics under different pump wavelengths are displayed in Fig. 7. All the samples containing GeSn exhibit subtle deviations in the early-time dynamics under 1600 nm wavelength excitation compared with those acquired with the 1251 nm pump. To illustrate it more precisely, temporal behavior within the initial 10 ps is plotted on a linear scale given in the relevant inserts. Note that when the optical pump is set to 1600 nm wavelength, the rise in induced THz absorption is faster and more pronounced compared to that of 1251 nm because the majority of carriers are generated directly to the Γ valley. Under 1251 nm wavelength pump excitation, electrons are also excited in other valleys; therefore, the rise time to maximum carrier density, corresponding to peak THz absorption, is reduced. In the Ge substrate, there are no clearly observed differences under both excitation wavelengths. Slightly resolved oscillations visible at 1600 nm excitation are probably related to the external circuitry noise, which becomes apparent at low signal intensities. In doped samples, the general decay picture shows no essential differences; however, a careful look at the inserts [panels (c)–(e)] allows us to resolve tiny details of carrier transport. A smooth peak of around 1 ps width can be distinguished at 1600 nm wavelength excitation and can be associated with the electrons' localization in the Γ valley. In Ge, it is about 3 ps.[66] However, here, in the GeSn structure, the valley localization time could be reduced due to the Sn atom-induced lattice stress. This is followed by a rapid decay on a 1.5 ps timescale caused by electron trapping from the Γ valley to ion-implantation-induced defects. Once the majority of defect states are filled, the THz absorption decreases more gradually and, when normalized, converges with the similar kinetics measured using a 1251 nm wavelength pump.

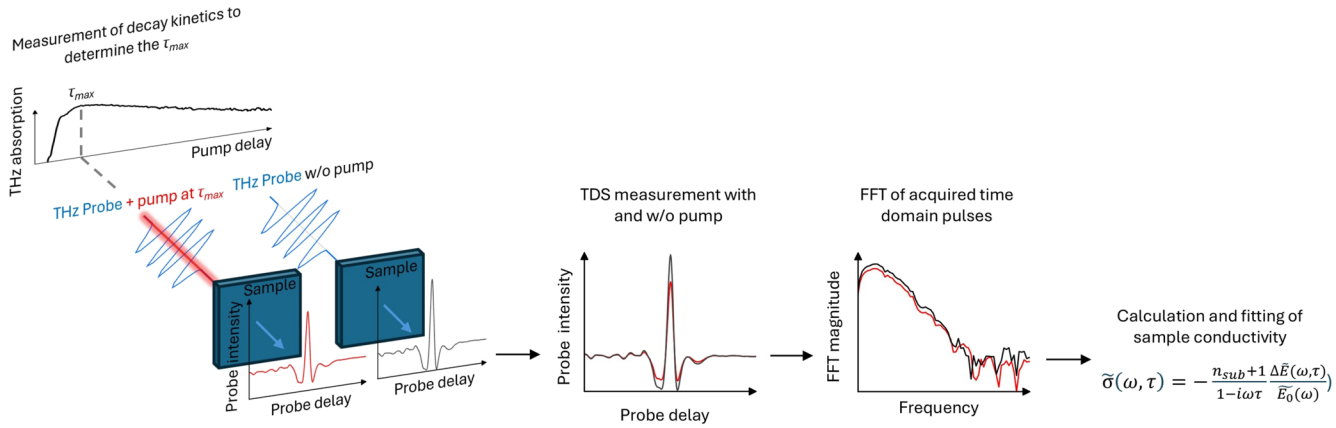

FIG. 8. Schematic representation of the optical-pump time-domain THz spectroscopy method used for the transient conductivity analysis. The step-by-step process is demonstrated as follows: determination of characteristic pump delay in the pump–probe decay spectra → measurement of sample transmitted THz probe pulses with and without pump at selected pump time delay → fast Fourier (FFT) of time-domain pulses → calculation of the transient conductivity → fitting the acquired data via selected model. For our research, the Drude–Smith model was used.

13 October 2026 07:58:21

© Author(s) 2026

It is especially evident in samples of 50 keV doping corresponding to the panels [(c) and (e)]. We hypothesize that this effect is related to inter-valley carrier scattering, which was observed earlier in pure Ge.[65] When the 1251 nm wavelength pump photon energy (0.99 eV) lies high above the direct energy gap of GeSn (0.68 eV), a large portion of the excited electrons are scattered to the higher effective mass L valley, which is confirmed by the PL spectra. The timescale of such processes lies in the femtosecond regime,[67] but, due to the limited time resolution of our setup (within 400 fs), they are not resolved.

2. Transient conductivity analysis

The transient conductivity profiles of the samples were extracted via Eq. (1) at the respective optical pump–THz probe delay at the maximum THz attenuation as schematically depicted in Fig. 8. As the real part and imaginary part of the complex conductivity stand for in-phase and out-of-phase characteristics of the carriers, obvious negative imaginary conductivity profiles of the samples in Fig. 9 suggest strong carrier backscattering behavior in the microscopic picture.[53] The fitting parameters of the Drude–Smith model on the samples, as well as the derived electrical constants, are presented in Table II.

First of all, one may notice the much higher mobility value extracted via THz spectroscopy compared to Hall effect measurement values reported in the literature, which usually fall around several hundreds of $cm^2\ V^{-1}\ s^{-1}$.[34,68,69] This discrepancy reflects the fundamental difference between carrier dynamics probed by ultrafast spectroscopy, such as THz spectroscopy, and steady-state characterization, such as Hall measurement.[42] On the one hand, Hall measurement is a macroscopic characterization technique performed on the scale of millimeters or centimeters. The carriers are forced to run across the whole material before contributing to the current readings; the likelihood of getting absorbed or scattered can be significantly affected by millimeter-scale grain boundaries. On the other hand, the carrier frequency of THz waves corresponds to a time frame of several picoseconds, and photocarriers usually transport for a few nanometers before the THz field flips the polarity. Thus, the conductivity profile probed by THz spectroscopy only considers intragrain backscattering events and can report higher values of mobility compared to those of the Hall effect.

The transient conductivity profile of the intrinsic sample, especially its negative imaginary conductivity, shows a classic signature of the Drude–Smith response. Together with the huge backscattering coefficient, it suggests notable carrier localization in intrinsic GeSn lattices, which could be attributed to its native defects.[61] However, due to its good crystallinity as revealed in Fig. 2 and PL emission in Fig. 4, its mobility is comparable to III–V materials, such as GaAs,[70] showcasing the feasibility of adopting GeSn alloys as material for fabricating high-speed electronics and THz photoconductive devices.

From the XRD results in Fig. 2 and weak PL efficiency in Fig. 4, we inferred that the substrate sample behaves as slightly amorphized Ge with negligible residual GeSn, whose crystallinity was slightly damaged during the dry-etching process, where ions were accelerated by RF coils to achieve highly anisotropic etching. Therefore, we observed more backscattering phenomena happening and smaller macroscopic mobility and subsequently its carrier lifetime. In addition, since the absorption coefficient of Ge is larger than that of GeSn at 1251 nm,[33] a higher photocarrier density in this sample can be expected.

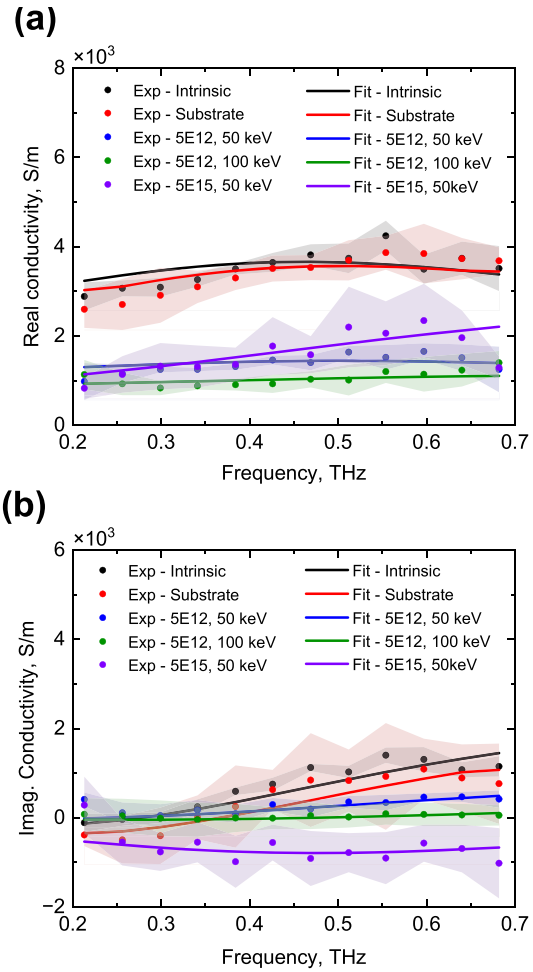

FIG. 9. Frequency-dependent transient conductivity profiles of the samples derived at their respective maximum attenuated pump–probe delay, illuminated by the optical pump centered at 1251 nm wavelength and 40 mW average power, fitted with the Drude–Smith model. Panels [(a) and (b)] present the real part and imaginary part of the complex conductivity. For clarity, the mean and standard deviation of the experimental data are denoted with solid dots and shaded regions, while the corresponding Drude–Smith fit curves are sketched with solid lines.

For the ion-implanted samples with lower dosages of 5×10^{12} cm^{-2}, their crystallinity is merely slightly damaged due to moderate ion bombardment, as shown in the XRD spectra of Fig. 3. Although the backscattering coefficients recorded in Table II of the samples are similar to the intrinsic benchmark, the results indicate that the origin of the carrier backscattering of GeSn alloys under mild implantation is still dominated by their native defects and grain boundaries. However, as revealed in the carrier lifetime (see Table I), the macroscopic DC conductivity, and mobility, a significant reduction can still be observed. Summarizing all these facts together, we can infer that the ion implantation likely created deep-level traps, which enhance the

13 October 2026 07:58:21

© Author(s) 2026

TABLE II. Drude–Smith fitting parameters and the derived macroscopic optoelectrical constants of the samples.

Sample	Intrinsic DC conductivity (S/cm)	Scattering time (fs)	Backscattering coefficient (−)	Macroscopic DC conductivity (S/cm)	Macroscopic mobility ($cm^2\ V^{-1}\ s^{-1}$)	Photocarrier concentration (cm^{-3})
intrinsic	68.36 ± 5.39	239 ± 17.4	−0.586 ± 0.023	28.20 ± 1.39	1447.8 ± 122.4	(1.23 ± 0.14) ×10^{17}
substrate	70.90 ± 10.4	245 ± 60.3	−0.659 ± 0.036	23.96 ± 1.77	1245.5 ± 410.3	(1.34 ± 0.59) ×10^{17}
5 × 10^{12}@50 keV	26.40 ± 1.56	203 ± 19.2	−0.548 ± 0.021	11.96 ± 1.07	1343.6 ± 84.20	(5.59 ± 0.68) ×10^{16}
5 × 10^{12}@100 keV	21.42 ± 3.67	135 ± 28.3	−0.580 ± 0.068	8.840 ± 0.90	852.30 ± 315.6	(7.19 ± 2.74) ×10^{16}
5 × 10^{15}@50 keV	56.28 ± 24.5	129 ± 32.2	−0.832 ± 0.065	9.360 ± 4.76	329.00 ± 184.3	(2.13 ± 1.52) ×10^{17}

rate of the Shockley–Read–Hall (SRH) recombination and rapidly drain out the conduction band, leading to reduced carrier densities compared to the intrinsic sample. Strikingly, the sample treated with a dosage of 5 × 10^{12} and an implantation energy of 100 keV possesses ps-level carrier lifetime, high mobility, and low carrier concentration simultaneously. This suggests that its ultrafast optoelectronic properties highly resemble a depleted high-speed photodiode or ion-implanted III–V epitaxial layer and, thus, could be regarded as a promising candidate for fabricating ultra-broadband THz detectors for either impulse or continuous-wave operation.[71–73]

The efficacy of the implantation energy on GeSn alloys can also be seen from this pair of samples. As shown in Table II, we observe a notable decrease in macroscopic mobility and DC conductivity in higher implantation energy (e.g., 100 keV). This can be expected as higher implantation energy would lead to greater damage to the crystallinity, which is supported by the XRD spectra in Fig. 3. Thus, a lower macroscopic mobility and DC conductivity can be explained. In addition, a slight rise in the carrier concentration could be attributed to Urbach's effect,[74] where amorphization of the crystal could lead to increased optical absorption in the longer wavelength region.

In contrast, the 5 × 10^{15}, 50 keV sample is in classic overdose conditions, with shattered GeSn crystallinity (see Fig. 3) and defects and impurities distributed all across the whole GeSn lattice leading to its complete amorphization. In particular, when compared to low-dosage samples, poor crystallinity significantly hinders the electron flow. Thus, we expect severe carrier backscattering, short carrier lifetime, and low macroscopic mobility in this sample. In contrast, the rise of photocarrier concentration can be explained by Urbach's effect.[74] As lattices go through amorphization, such as intense ion implantation, their bandgap structure is largely distorted, leading to a higher likelihood of photons with lower photon energy being absorbed. Therefore, with more optical absorption pathways, a higher photocarrier density in this sample can be expected. The derived electrical constants in Table II validate these expectations. Taking into account the calculated pump excitation density and the photocarrier concentration obtained from conductivity fitting, we can also estimate the excitation efficiency, which, depending on the sample, lies in the 20%–70% regime. During our investigation, the experimental complex conductivity is well-fitted by the Drude–Smith model. This suggests that the conductivity is still predominantly governed by carrier transport, albeit affected by strong localization; extra care should be taken when studying near-amorphized samples or noncrystalline media. The literature has reported that in amorphous samples, phonon-assisted hopping could take over the majority of the contribution to conductivity, rather than classic carrier transport.[75] In this case, the Drude–Smith model could fail to correctly evaluate the optoelectronic properties of these samples.

IV. CONCLUSIONS

To summarize, we present the first optical pump–THz probe spectroscopy and transient conductivity analysis of the unannealed ion-implanted GeSn, revealing its ultrafast optoelectronic characteristics under various defect-engineered conditions covering implantation energy and doping level. Complementary characterization tools, such as x-ray diffraction and photoluminescence, were used to examine the samples' crystallinity and bandgap structures. The XRD measurements revealed the distinct GeSn crystalline film peak at 65.32°, along with the expected peaks from the underlying Ge-VS layer and substrate. The PL analysis of the intrinsic GeSn layer exhibited dual-valley emission, producing two peaks at 0.61 and 0.675 eV, which correspond to radiative transitions from the L-valley and Γ-valley, respectively. As the unannealed ion-implanted GeSn alloys have been demonstrated as a promising candidate for fabricating photoconductive THz devices,[33,34] this work lays a solid foundation for assessing the ultrafast optoelectronic properties of the defect-engineered GeSn. In particular, the investigated mildly implanted samples show both picosecond-level characteristic carrier lifetimes of 8.3 and 4.5 ps for implantation energies of 50 and 100 keV, respectively, together with remarkably high transient mobilities ranging from 1340 to 850 $cm^2\ V^{-1}\ s^{-1}$. While these values are comparable to those of commonly used III–V materials, which have mobilities in the range of ≈300 $cm^2\ V^{-1}\ s^{-1}$ for low-temperature-grown GaAs[76] and around 2000 $cm^2\ V^{-1}\ s^{-1}$ in the case of InGaAs.[77] These materials, in contrast to GeSn, are not compatible with the CMOS foundry process. Thus, these characteristics indicate good material quality of the GeSn samples and highlight their strong potential as candidates for the fabrication of photoconductive THz detectors.

In the intrinsic sample, owing to its good crystallinity, 132 ps sub-ns characteristic carrier lifetime and high transient macroscopic mobility of 1448 $cm^2\ V^{-1}\ s^{-1}$ were found. In addition, the −0.586 backscattering coefficient suggested the existence of native defects and grain boundaries in RPCVD-grown GeSn lattices. In contrast, the substrate sample, which is selected to provide a comparison with other conventional group IV thin films, shows a more pronounced

13 October 2026 07:58:21

© Author(s) 2026

backscattering with a coefficient value of −0.659, smaller macroscopic mobility at 1246 $cm^2\ V^{-1}\ s^{-1}$, and a slightly higher carrier concentration. The former two properties could be attributed to the damage from dry etching during the preparation of this sample, while the concentration rise likely comes from the higher optical absorption coefficient near the 1251 nm wavelength in Ge than in GeSn.

Regarding the ion implantation samples, when they are moderately treated, such as the 5×10^{12} samples, ion implantation reaches an optimal balance between the carrier lifetime, crystallinity, and mobility. In this regard, the 5×10^{12}, 50 keV sample was found to exhibit picosecond-level carrier lifetime of 8.3 ps, good crystallinity, and high mobility close to the intrinsic sample (1344–1448 $cm^2\ V^{-1}\ s^{-1}$), underlining its potential for future applications in high speed SWIR, MIR detectors, THz photoconductive detectors, and optoelectronic transceivers. However, as the implantation energy increases, such as the 5×10^{12}, 100 keV sample, the mobility starts to diminish, and the backscattering phenomenon increases, due to additional damage imposed on the lattice from higher implantation energy. Conversely, the 5×10^{15}, 50 keV sample shows a picture of amorphization in the lattice structure. Therefore, we observe a near-amorphous sample with severe backscattering of −0.832, comparatively low carrier mobility, yet the highest carrier density of all the samples. While the former two properties are classic signatures of an amorphous lattice, the increment in carrier concentration may be explained by the Urbach's effect.

Future investigations will further focus on relating the transient optoelectronic properties of the samples to functional devices, particularly through THz emission spectroscopy and fabrication of defect-engineered GeSn-based photoconductive devices. In particular, the low-dose implanted samples where the exceptional carrier mobility makes them an ideal material for broadband mid-infrared or THz detectors are of particular interest. With this in mind, we expect that the findings reported in this work could further advance the development of CMOS-compatible THz optoelectronics, including but not limited to mass-producible THz photoconductive devices, THz system-on-chips (SoC) for spectroscopic studies, or miniaturized 6 G communication transceivers.

ACKNOWLEDGMENTS

The authors would like to acknowledge Taiwan Semiconductor Research Institute for insightful discussion on the growth condition and properties of the RPCVD-grown GeSn, providing the samples and the ion implantation; Mr. Cheng-Siang Le and Mr. Zi-Xiang Liao at Institute of Electronic Engineering, National Tsing Hua University, Taiwan, for handling the GeSn samples and developing the dry etching recipes; Dr. Le Thi Quynh at the Center for Nanotechnology, Materials Science, and Microsystems, National Tsing Hua University, Taiwan, and Dr. Sandra Stanionytė at Center of Physical Sciences and Technology (FTMC), Vilnius, Lithuania, for the XRD measurements and their analysis. Special thanks go to Dr. Evelina Dudutienė (FTMC, Vilnius, Lithuania) for her kind assistance in photoluminescence-related experiments. This research is supported by the National Science and Technology Council, under Grant Nos. "112-2221-E-007-089-MY3" and "113-2628-E-007-011-MY3."

AUTHOR DECLARATIONS

Conflict of Interest

The authors have no conflicts to disclose.

Author Contributions

S.D. and C.-M. contributed equally to this work.

Simonas Driukas: Conceptualization (equal); Data curation (equal); Investigation (equal); Visualization (lead); Writing – original draft (lead); Writing – review & editing (equal). **Chia-Ming Mai**: Conceptualization (equal); Data curation (equal); Investigation (equal); Visualization (supporting); Writing – original draft (lead); Writing – review & editing (equal). **Ričardas Norkus**: Investigation (supporting); Writing – review & editing (supporting). **Bronislavas Čechavičius**: Investigation (equal). **Ignas Nevinskas**: Writing – review & editing (supporting). **Shang-Hua Yang**: Conceptualization (equal); Supervision (equal); Writing – review & editing (equal). **Gintaras Valušis**: Conceptualization (equal); Supervision (equal); Writing – original draft (supporting); Writing – review & editing (equal).

DATA AVAILABILITY

The data that support the findings of this study are available from the corresponding author upon reasonable request.

REFERENCES

[1] A. Leitenstorfer, A. S. Moskalenko, T. Kampfrath, J. Kono, E. Castro-Camus, K. Peng, N. Qureshi, D. Turchinovich *et al.*, J. Phys. D: Appl. Phys. **56**, 223001 (2023).
[2] T. Nagatsuma, G. Ducournau, and C. C. Renaud, Nat. Photonics **10**, 371 (2016).
[3] Y. Huang, Y. Shen, and J. Wang, Engineering **22**, 106 (2023).
[4] G. Valušis, A. Lisauskas, H. Yuan, W. Knap, and H. G. Roskos, Sensors **21**, 4092 (2021).
[5] A. Krotkus, J. Phys. D: Appl. Phys. **43**, 273001 (2010).
[6] C. W. Berry, N. Wang, M. R. Hashemi, M. Unlu, and M. Jarrahi, Nat. Commun. **4**, 1622 (2013).
[7] S.-H. Yang, M. R. Hashemi, C. W. Berry, and M. Jarrahi, IEEE Trans. Terahertz Sci. Technol. **4**, 575 (2014).
[8] S. H. Yang and M. Jarrahi, Appl. Phys. Lett. **107**, 131111 (2015).
[9] N. Dyakonova, A. El Fatimy, J. Łusakowski, W. Knap, M. I. Dyakonov, M. A. Poisson, E. Morvan, S. Bollaert, A. Shchepetov, Y. Roelens, C. Gaquiere, D. Theron, and A. Cappy, Appl. Phys. Lett. **88**, 141906 (2006).
[10] T. Maekawa, H. Kanaya, S. Suzuki, and M. Asada, Appl. Phys. Express **9**, 024101 (2016).
[11] I. Kasalynas, R. Venckevicius, and G. Valušis, IEEE Sens. J. **13**, 50 (2013).
[12] I. Kašalynas, D. Seliuta, R. Simniškis, V. Tamošiūnas, K. Köhler, and G. Valušis, Electron. Lett. **45**, 833 (2009).
[13] G. Liang, T. Liu, and Q. J. Wang, IEEE J. Sel. Top. Quantum Electron. **23**, 1200118 (2017).
[14] M. S. Vitiello and P. De Natale, Adv. Quantum Technol. **5**, 2100082 (2022).
[15] T. Onishi, T. Tanigawa, and S. Takigawa, Appl. Phys. Lett. **97**, 092117 (2010).
[16] V. Jakštas, I. Grigelionis, V. Janonis, G. Valušis, I. Kašalynas, G. Seniutinas, S. Juodkazis, P. Prystawko, and M. Leszczyński, Appl. Phys. Lett. **110**, 202101 (2017).

13 October 2026 07:58:21

© Author(s) 2026

[17]H. Qin, X. Li, J. Sun, Z. Zhang, Y. Sun, Y. Yu, X. Li, and M. Luo, Appl. Phys. Lett. **110**, 171109 (2017).
[18]M. Bauer, A. Ramer, S. A. Chevtchenko, K. Y. Osipov, D. Cibiraite, S. Pralgauskaite, K. Ikamas, A. Lisauskas, W. Heinrich, V. Krozer, and H. G. Roskos, IEEE Trans. Terahertz Sci. Technol. **9**, 430 (2019).
[19]P. Hillger, J. Grzyb, R. Jain, and U. R. Pfeiffer, IEEE Trans. Terahertz Sci. Technol. **9**, 1 (2019).
[20]D. B. But, A. V. Chernyadiev, K. Ikamas, C. Kołaciński, A. Krysl, H. G. Roskos, W. Knap, and A. Lisauskas, Opto-Electron. Rev. **31**, e144599 (2023).
[21]J. Taraci, S. Zollner, M. R. McCartney, J. Menendez, M. A. Santana-Aranda, D. J. Smith, A. Haaland, A. V. Tutukin, G. Gundersen, G. Wolf, and J. Kouvetakis, J. Am. Chem. Soc. **123**, 10980 (2001).
[22]S. Wirths, D. Buca, and S. Mantl, Prog. Cryst. Growth Charact. Mater. **62**, 1 (2016).
[23]S. Zaima, O. Nakatsuka, N. Taoka, M. Kurosawa, W. Takeuchi, and M. Sakashita, Sci. Technol. Adv. Mater. **16**, 043502 (2015).
[24]J. Zheng, Z. Liu, C. Xue, C. Li, Y. Zuo, B. Cheng, and Q. Wang, J. Semicond. **39**, 061006 (2018).
[25]Y. Miao, G. Wang, Z. Kong, B. Xu, X. Zhao, X. Luo, H. Lin, Y. Dong, B. Lu, L. Dong, J. Zhou, J. Liu, and H. H. Radamson, Nanomaterials **11**, 2556 (2021).
[26]W. Wang, D. Lei, Y.-C. Huang, K. H. Lee, W.-K. Loke, Y. Dong, S. Xu, C. S. Tan, H. Wang, S.-F. Yoon, X. Gong, and Y.-C. Yeo, Opt. Express **26**, 10305 (2018).
[27]D. Lei, K. H. Lee, Y. C. Huang, W. Wang, S. Masudy-Panah, S. Yadav, A. Kumar, Y. Dong, Y. Kang, S. Xu, Y. Wu, C. S. Tan, X. Gong, and Y. C. Yeo, IEEE Trans. Electron Devices **65**, 3754 (2018).
[28]D. Stange, S. Wirths, R. Geiger, C. Schulte-Braucks, B. Marzban, N. von den Driesch, G. Mussler, T. Zabel, T. Stoica, J. M. Hartmann, S. Mantl, Z. Ikonic, D. Grützmacher, H. Sigg, J. Witzens, and D. Buca, ACS Photonics **3**, 1279 (2016).
[29]J. Mathews, Z. Li, Y. Zhao, J. Gallagher, I. Agha, J. Menendez, and J. Kouvetakis, ECS Trans. **75**, 163 (2016).
[30]G. E. Chang, S. Q. Yu, J. Liu, H. H. Cheng, R. A. Soref, and G. Sun, IEEE J. Sel. Top. Quantum Electron. **28**, 3800611 (2022).
[31]S. Ghosh, G. Sun, S.-Q. Yu, and G.-E. Chang, IEEE J. Sel. Top. Quantum Electron. **31**, 3800211 (2025).
[32]W.-C. Chen and S.-H. Yang, Opt. Express **30**, 31742 (2022).
[33]W.-C. Chen, C.-W. Chang, and S.-H. Yang, Opt. Lett. **47**, 4411 (2022).
[34]Wang-Chien Chen, Pin-Han Lee, Pouya Torkaman, and Shang-Hua Yang, "Germanium–Tin (GeSn) terahertz photoconductive detector," ACS Photonics **13**, 1609–1616 (2025).
[35]N. M. Burford and M. O. El-Shenawee, Opt. Eng. **56**, 010901 (2017).
[36]M. Naftaly, N. Vieweg, and A. Deninger, Sensors **19**, 4203 (2019).
[37]X. Fu, Y. Liu, Q. Chen, Y. Fu, and T. J. Cui, Front. Phys. **10**, 869537 (2022).
[38]S.-G. Park, Y. Choi, Y.-J. Oh, and K.-H. Jeong, Opt. Express **20**, 25530 (2012).
[39]R. J. B. Dietz, B. Globisch, H. Roehle, D. Stanze, T. Göbel, and M. Schell, Opt. Express **22**, 19411 (2014).
[40]A. Fekecs, M. Bernier, D. Morris, M. Chicoine, F. Schiettekatte, P. Charette, and R. Arès, Opt. Mater. Express **1**, 1165 (2011).
[41]O. Lindberg, Proc. IRE **40**, 1414 (1952).
[42]B. G. Alberding, W. R. Thurber, and E. J. Heilweil, J. Opt. Soc. Am. B **34**, 1392 (2017).
[43]T. He, B. Zhang, G. C. Wang, M. D. Zang, Y. B. Hou, and J. L. Shen, J. Phys. D: Appl. Phys. **49**, 075111 (2016).
[44]G. Jnawali, Y. Rao, H. Yan, and T. F. Heinz, Nano Lett. **13**, 524 (2013).
[45]J. B. Baxter and C. A. Schmuttenmaer, in *Terahertz Spectroscopy*, edited by S. L. Dexheimer (CRC Press, 2017), pp. 73–118.
[46]J. Neu, APL Photonics **8**, 071103 (2023).
[47]R. Ulbricht, E. Hendry, J. Shan, T. F. Heinz, and M. Bonn, Rev. Mod. Phys. **83**, 543 (2011).
[48]M. Tinkham, Phys. Rev. **104**, 845 (1956).
[49]H. K. Nienhuys and V. Sundström, Phys. Rev. B **71**, 235110 (2005).
[50]J. Dai, J. Zhang, W. Zhang, and D. Grischkowsky, J. Opt. Soc. Am. B **21**, 1379 (2004).
[51]A. D. Bristow, N. Rotenberg, and H. M. van Driel, Appl. Phys. Lett. **90**, 191104 (2007).
[52]N. V. Smith, Phys. Rev. B **64**, 155106 (2001).
[53]C. S. Yang, M. H. Lin, C. H. Chang, P. Yu, J. M. Shieh, C. H. Shen, O. Wada, and C. L. Pan, IEEE J. Quantum Electron. **49**, 677 (2013).
[54]S. Wirths *et al.*, Nat. Photonics **9**, 88 (2015).
[55]T. D. Eales, I. P. Marko, S. Schulz, E. O'Halloran, S. Ghetmiri, W. Du, Y. Zhou, S. Q. Yu, J. Margetis, J. Tolle, E. P. O'Reilly, and S. J. Sweeney, Sci. Rep., **9**(1), 14077 (2019).
[56]M. Lundstrom, *Fundamentals of Carrier Transport*, 2nd ed. (Cambridge University Press, 2000), Chap. 1.
[57]S. M. Sze and K. K. Ng, *Physics of Semiconductor Devices*, 3rd ed. (John Wiley & Sons, 2006).
[58]H. Ye and J. Yu, Sci. Technol. Adv. Mater. **15**, 024601 (2014).
[59]E. Tiesinga, P. J. Mohr, D. B. Newell, and B. N. Taylor, Rev. Mod. Phys. **93**, 025010 (2021).
[60]Y. S. Suh, M. S. Carroll, R. A. Levy, M. A. Sahiner, G. Bisognin, and C. A. King, IEEE Trans. Electron Devices **52**, 91 (2005).
[61]A. Giunto and A. Fontcuberta i Morral, Appl. Phys. Rev. **11**, 041333 (2024).
[62]X. Liu, A. Giunto, J. D. Hutchinson, N. Humblot, D. Damry, R. L. Milot, A. F. i. Morral, and J. Boland, in *2022 47th International Conference on Infrared, Millimeter and Terahertz Waves (IRMMW-THz)* (IEEE, 2022), pp. 1–2.
[63]E. Vitiello, S. Rossi, C. A. Broderick, G. Gravina, A. Balocchi, X. Marie, E. P. O'Reilly, M. Myronov, and F. Pezzoli, Phys. Rev. Appl. **14**, 064068 (2020).
[64]M. K. Hudait, S. W. Johnston, M. B. Clavel, S. Bhattacharya, S. Karthikeyan, and R. Joshi, J. Mater. Chem. C **10**, 10530 (2022).
[65]R. Norkus, I. Nevinskas, and A. Krotkus, J. Appl. Phys. **126**, 225704 (2019).
[66]A. Urbanowicz, R. Adomavičius, A. Krotkus, and V. L. Malevich, Semicond. Sci. Technol. **20**, 1010 (2005).
[67]S. Zollner, K. D. Myers, K. G. Jensen, J. M. Dolan, D. W. Bailey, and C. J. Stanton, Solid State Commun. **104**, 51 (1997).
[68]K. Tien, Y. Chen, C. Liu, H. Kao, and J. Li, Adv. Electron. Mater. **11**, 2400925 (2025).
[69]Y. Junk, O. Concepción, M. Frauenrath, J. Sun, J. H. Bae, F. Bärwolf, A. Mai, J. Hartmann, D. Grützmacher, D. Buca, and Q. Zhao, Adv. Electron. Mater. **11**, 2400561 (2025).
[70]M. C. Beard, G. M. Turner, and C. A. Schmuttenmaer, Phys. Rev. B **62**, 15764 (2000).
[71]T.-A. Liu, M. Tani, M. Nakajima, M. Hangyo, and C.-L. Pan, Appl. Phys. Lett. **83**, 1322 (2003).
[72]T.-A. Liu, M. Tani, M. Nakajima, M. Hangyo, K. Sakai, S.-I. Nakashima, and C.-L. Pan, Opt. Express **12**, 2954 (2004).
[73]K. Moon, E. S. Lee, I.-M. Lee, D. W. Park, and K. H. Park, Appl. Phys. Lett. **112**, 031102 (2018).
[74]F. Urbach, Phys. Rev. **92**, 1324 (1953).
[75]N. F. Mott and E. A. Davis, *Electronic Processes in Non-Crystalline Materials*, 2nd ed. (Oxford University Press, Oxford, 1979), Chap. 1.
[76]L. Hou and W. Shi, IEEE Trans. Electron Devices **60**, 1619 (2013).
[77]D. V. Lavrukhin, A. E. Yachmenev, Y. G. Goncharov, K. I. Zaytsev, R. A. Khabibullin, A. M. Buryakov, E. D. Mishina, and D. S. Ponomarev, IEEE Trans. Terahertz Sci. Technol. **11**, 417 (2021).

13 October 2026 07:58:21

© Author(s) 2026